

Learning Continuous Cost-to-Go Functions for Non-holonomic Systems

Jinwook Huh, Daniel D. Lee and Volkan Isler

Abstract—This paper presents a supervised learning method to generate continuous cost-to-go functions of non-holonomic systems directly from the workspace description. Supervision from informative examples reduces training time and improves network performance. The manifold representing the optimal trajectories of a non-holonomic system has high-curvature regions which can not be efficiently captured with uniform sampling. To address this challenge, we present an adaptive sampling method which makes use of sampling based planners along with local, closed-form solutions to generate training samples. The cost-to-go function over a specific workspace is represented as a neural network whose weights are generated by a second, higher order network. The networks are trained in an end-to-end fashion. In our previous work, this architecture was shown to successfully learn to generate the cost-to-go functions of holonomic systems using uniform sampling. In this work, we show that uniform sampling fails for non-holonomic systems. However, with the proposed adaptive sampling methodology, our network can generate near-optimal trajectories for non-holonomic systems while avoiding obstacles. Experiments show that our method is two orders of magnitude faster compared to traditional approaches in cluttered environments.

I. INTRODUCTION

Non-holonomic constraints of a system are non-integrable kinematic constraints involving the derivatives of the system’s state variables. For example, a simple car, whose state can be represented as position and orientation on a plane, is subject to a turning constraint: it cannot instantaneously change its orientation to an arbitrary angle. Hence, the magnitude of the derivative of the orientation is upper-bounded. Non-holonomic constraints are inherent to the system’s kinematics and cannot be removed using algebraic tricks. A classical example of a non-holonomic robotics system is the Dubin’s car [1] which can go forward and change its orientation subject to a maximum curvature constraint. This constraint can also be expressed as a lower bound on the turning radius. The Reeds-Shepp car [2] is slightly more general: it can flip its motion direction (i.e. back up) but it must still satisfy the curvature constraint when moving.

It is possible to compute optimal solutions for non-holonomic systems for some special cases. For example, for the Dubins car, it was shown that the optimal solution between two configurations is composed of at most three segments where each segment is either a line segment or an arc of the unit circle where the unit corresponds to the minimum turning radius [1]. In other words, the car either goes straight or turns at maximum curvature. This structure allows for computing the optimal solution simply

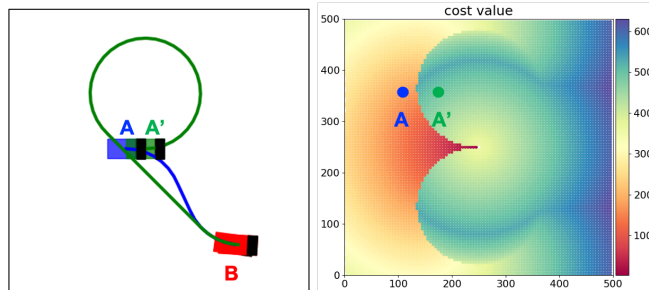


Fig. 1: (Left) Configuration A' is obtained by slightly perturbing A . The cost of A' to the goal B is drastically different from the cost between A and B . (Right) A and A' are in the region with high curvature of cost-to-go.

by enumerating combinatorially different paths and picking the best one (Once the combinatorial structure is fixed, the path itself can be computed using elementary geometry.) A similar solution structure is also known for the Reeds-Shepp car [2].

Motion planning for non-holonomic systems in general is difficult. In the presence of obstacles, the optimal solution no longer satisfies the structural properties mentioned above. For example, even in the case of turning a corner with a Dubins car, turning with maximum curvature may not be optimal [3]. To see why non-holonomic systems are challenging for commonly used sampling-based planners such as RRT and variants, it is helpful to visualize the space of allowable trajectories as a manifold where neighborhoods are formed by connecting nearby configurations satisfying the non-holonomic constraint. Now, consider the example in Fig. 1 where the initial configuration A and the goal configuration B have the same orientation but different positions. The geodesic distance between these two configurations is relatively small as can be seen from the figure. Next, imagine slightly perturbing A to the configuration A' as shown in the figure. The shortest path from A' to B is drastically longer. This means that configurations A , A' and B lie in a region with high curvature. Capturing the connectivity of such regions with sampling based planners is difficult because sampling a small number of “nearby” points may not be sufficient to connect such local regions [4]–[7].

In our recent work, we introduced a novel path planning approach where we use cost-to-go values obtained from a traditional planner to fit a continuous cost-to-go function over the configuration space (C-space) represented as a neural network. We then showed that we can train a higher order network which can directly output this function from a representation (e.g. a picture) of the robot’s workspace. In [8]

we showed that after training, our approach can be used to compute continuous trajectories almost instantaneously and generalizes well across workspaces. In the present work, we seek to extend this approach to non-holonomic systems.

Unfortunately, the existence of high-curvature regions on the motion planning manifold also makes it difficult for our approach to efficiently represent the cost-to-go function using uniform sampling.

In this paper, we show how this difficulty can be overcome using an adaptive sampling approach. Specifically, we present an adaptive sampling methodology based on sampling according to the curvature of cost-to-go. The suggested approach allows the network to learn cost-to-go efficiently and to output continuous cost-to-go functions in C-space from a workspace input. The planner with the cost-to-go function network rapidly generates near-optimal trajectories satisfying constraints and avoiding obstacles in cluttered environments. We demonstrate that our approach is orders of magnitude faster than traditional approaches for trajectory generation in cluttered environments.

II. RELATED WORK

Many robotics applications necessitate motion planning to move a system from one configuration to another configuration while satisfying constraints and avoiding obstacles [9]–[11]. Robotic systems such as car-like robots are subject to inherent non-holonomic constraints by kinematics. These constraints make motion planning more difficult since two feasible configurations may not be directly connected via a C-space shortest path due to kinematic constraints.

For a simple car model in free space, Dubins [1] and Reeds and Shepp [2] showed that there the shortest path for the respective systems can be expressed as a combination of a small number of arc turning and straight line primitives. However, there is no analytical solution to the shortest path problem when such systems operate in cluttered environments.

Solutions for non-holonomic motion planning in cluttered environments include traditional lattice-based planners which apply discrete search with a sequence of predefined control primitives [12]. Rapidly-exploring Random Tree (RRT) planners solve kinodynamic problems [4] by randomly exploring on C-space with random continuous control inputs. However, in non-holonomic systems, they require exhaustive random samples and collision checks as well as post-processing for smoothing [13], [14].

Although there are many approaches to the optimal trajectory for non-holonomic systems such as navigation functions [15], [16] and differential dynamic programming [17], these approaches are vulnerable to local minima and difficult to tune parameters in cluttered environments.

Recently, deep neural networks have been proposed for motion planning. Tamar et al. suggest a value iteration network, which is a similar concept to learning cost-to-go. They do not address non-holonomic constraints [18]. Motion planning network [19] outputs preliminary trajectories for traditional planners and it is extensible to the problem with

non-holonomic constraints [20]. In addition, there are some deep neural networks for good sample distributions [21]–[24]. Zeng et al. [25] suggests a neural network which outputs cost volumes for computing costs of sample trajectories. The planner chooses a minimum cost trajectory among sample trajectories. These neural network approaches show performance improvement over traditional planners using modern deep neural networks. However, they use uniform samples from trajectories by traditional planners or human demonstrations for network training without considering sample efficiency.

In general, training network for motion planning requires a massive dataset, since a trajectory is generated by a sequence of control inputs. Therefore, many previous neural network approaches exploit successful trajectories by traditional motion planners to create training datasets [19]–[21], [23], [24]. However, all data samples are not equally important for the training of neural networks [26], [27]. Adaptive sampling or boosting can accelerate training and improve performance. Although there are some classical approaches on adaptive sampling for sampling based planners [28]–[30], most neural network approaches for motion planning do not handle the issue of sampling to improve the performance of training. Our primary contribution to neural network based motion planning is a novel adaptive sampling method which captures high curvature regions of cost-to-go for the non-holonomic systems but using a combination of RRT based and optimal, closed-form local planners.

III. PROBLEM STATEMENT

Our representative non-holonomic system is a Reeds-Shepp car with a minimum turning radius ρ [31]. Its configuration space is given by $\mathcal{C} = \mathbb{R}^2 \times \mathbb{S}^1$. A configuration $q \in \mathcal{C}$ is denoted as $q = (x, y, \theta)$ and its time derivative $\dot{q} = (\dot{x}, \dot{y}, \dot{\theta})$. The system has a nonholonomic constraint such that $\dot{x} \cos \theta - \dot{y} \sin \theta = 0$. The control input u has longitudinal velocity, steering angle, and gear direction for forward and backward directions.

The cost-to-go function is a real-valued function $L(q)$ on the configuration space $q \in \mathcal{C}$. The optimal control input can be as satisfies,

$$u_k^*(q_k, q_{\text{goal}}) = \arg \min_{u'} \{l(q_k, u') + L^*(q_{k+1}, q_{\text{goal}})\},$$

$$q_{k+1} = g(q_k, u)$$

where $l(q_k, u')$ is a constant cost given control input u , q_{goal} is a goal configuration, g is forward kinematics function of the system, and $L^*(q_{k+1})$ is the minimum cost-to-go value at q_{k+1} . In this paper, we define the cost of a collision-free path as the length of the path.

Although algorithms to generate optimal Dubins and Reeds-Shepp curves exist for environments with no obstacles, there is no analytical solution to the shortest path problem in cluttered environments. There are a few special cases to solve the problem. Agarwal et al. [32] solve the shortest path problem inside polygonal obstacles. Koval and

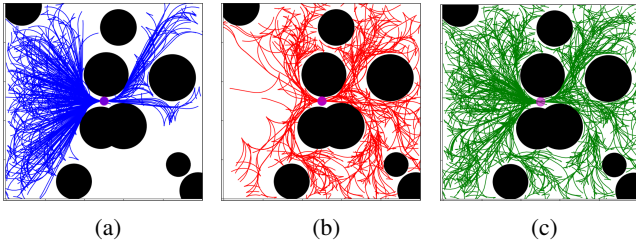


Fig. 2: Two phase tree expansion. (a) Initial collision-free branches by Reeds-Shepp curves. (b) Additionally generated branches by RRT* for exploring unreachable areas. (c) The entire tree structure.

Isler [3] show that the optimal solution does not necessarily turn at the maximum curvature.

For a specific workspace \mathcal{W} , the cost-to-go (c2g) function returns the cost between two configurations $f_{\mathcal{W}} : \mathcal{C} \times \mathcal{C} \rightarrow [0, \infty)$. Specifically, the function $f_{\mathcal{W}}$ is a cost-to-go function for any given configurations s and t in the configuration space \mathcal{C} , which returns the cost for the nonholonomic system to traverse a collision-free path while satisfying the nonholonomic constraint from s to t . We train a network to output a function of cost-to-go instead of cost-to-go values on \mathcal{C} -space.

Since the cost-to-go is a result of a sequence of control inputs between two configurations and it is not a simple Euclidean distance between them, the cost-to-go function is not efficiently trained with a set of points distributed uniformly over the \mathcal{C} -space. Therefore, we also focus on effective dataset generation for efficient training of the network.

IV. DATASET GENERATION WITH ADAPTIVE SAMPLING

This section presents the details of our methodology for adaptive sampling.

The success of our approach relies on generating a dataset which captures high curvature regions on the motion planning manifold. Our dataset consists of workspace instances represented as point clouds of obstacles (or a workspace image) along with a list of triplets composed of source and destination configurations and the associated cost to go.

We start with generating random workspaces. For each workspace, we run RRT* with randomly initialized seed configurations until the generated trajectories cover the entire configuration space. In addition, we apply optimal Reeds-Shepp curves for paths to connect local nodes [1], [2], [33].

We sample a pair of points (s, t) and the corresponding cost on the same branch of trees as shown in Fig. 3(a). Since a sub-path of an optimal path is also optimal and we assume that paths from RRT* converges to optimal paths asymptotically, the corresponding cost of these sampled configurations also has the minimum cost between them.

To handle the angle wrapping, the orientation θ is mapped into $(\cos(\theta), \sin(\theta))$, and positions x and y are normalized to $[0, 1]$.

Next, we describe the three factors critical to the performance of the dataset: diversity with respect to workspace,

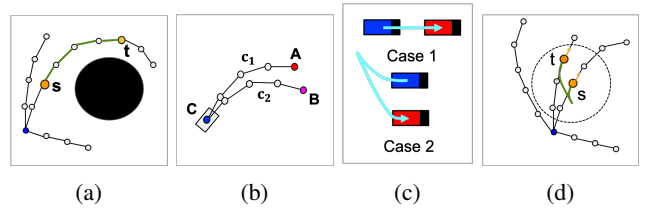


Fig. 3: Sample generation. (a) We sample a pair of configurations (s, t) on the same branch of RRT*. (b) The cost-to-go between A and B along the tree does not reflect the min. cost (c) A start configuration is a blue rectangle, and a goal configuration is a red rectangle with orientations indicated by black tips. Case 2 has a higher cost-to-go than Case 1 due to constraints. (d) To capture cases like (c), additional cost-to-go samples across vertices of RRT* within a threshold distance are generated.

non-holonomic constraints, and maximizing total information.

A. Two phase tree construction

We propose an efficient two phase tree construction method for RRT* as shown in Fig. 2. First, we generate an initial tree with collision-free Reeds-Shepp curves from a seed (Fig. 2(a)). Next, an RRT* starts exploring with this initial tree towards unexplored areas. Fig. 2(b) shows additionally explored branches in the second step and Fig. 2(c) shows the constructed tree including all branches generated in the first and second steps.

Since branches in the initial tree by Reeds-Shepp curves (Fig. 2(a)) are optimal, the RRT* keeps the optimality by rewiring routines with only newly explored nodes and branches. This approach reduces the computation time of RRT* and the tree covers the whole configuration space effectively (Fig. 2(c)).

B. Dataset for non-holonomic constraints

Although we generate 10,000 workspace instances and 50,000 pairwise configurations for each instance by RRT* for diversity in various environments, we need additional effective data samples caused by non-holonomic constraints. Specifically, the dataset must capture paths across branches of the tree created in the previous section.

In Fig. 3(b), although the dataset from RRT* includes information of the cost c_1 from A to C and the cost c_2 from A to C , it doesn't include the cost between A and C . The costs c_1 and c_2 contain important information for collision avoidance. The cost between A and C is also informative due to non-holonomic constraints. In Fig. 3(c), Case 1 and Case 2 have the same Euclidean distance, but the non-holonomic constraint makes a difference in cost-to-go values of the two cases. Since RRT* expands the tree in the longitudinal direction to keep optimality by rewiring, it is difficult to include such samples in the dataset.

Therefore, we additionally sample cost-to-go across vertices of RRT* computed by Reeds-Shepp curves as shown in Fig. 3(d). We sample pairs of vertices within a threshold

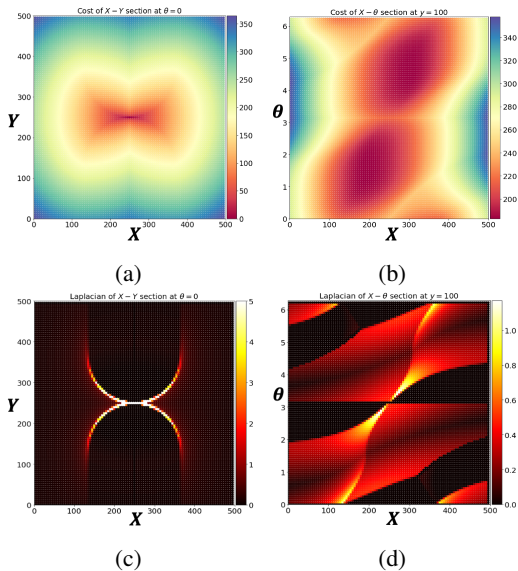


Fig. 4: Visualization of cost-to-go for the goal configuration at $(250, 250, 0)$ (a) $X - Y$ plane with $\theta = 0$ (b) $X - \theta$ plane with $y = 100$ (c) Laplacian of cost-to-go shown in (a) (d) Laplacian of cost-to-go shown in (b) (Best viewed in color).

distance $\alpha * \rho$, where α is a constant ($\alpha = 1.5$ in this paper) and ρ is a lower bounded turning radius by the non-holonomic constraint. In the region outside of the turning radius, the cost for collision avoidance is more dominant as shown in trained cost-to-go images (Fig. 8).

C. Adaptive sampling based on diversity of gradient

As described in [26], [27], all data samples are not equally critical for the neural network performance. A good dataset can accelerate the training and impact the performance of the network. Uniform sampling can cover the whole space, but it leads to including redundant data due to biased data distribution. Therefore, we need an additional effective sampling strategy since non-holonomic constraints “curve” the manifold of cost-to-go as shown in Fig. 1. We can see that the cost-to-go is distinct from Euclidean distance due to the non-holonomic constraint even without an obstacle in Fig. 4(a) and 4(b). Therefore, we need to consider the curvature of cost-to-go, since uniform sampling is difficult to represent the manifold of cost-to-go.

We consider the curvature of cost-to-go by calculating its Laplacian, shown in Figs. 4(c) and 4(d) without obstacles. We need dense sampling around high Laplacian areas since high Laplacian means high curvature. We can see that regions around goal configuration have higher Laplacian. In environments with obstacles, since it is hard to compute the Laplacian directly, we compute a ratio of the cost-to-go gradient to the Euclidean distance gradient. Practically, if this ratio is high, we sample more with high probability. Fig. 5 shows ratio of samples histograms based on uniform sampling and adaptive sampling. The ratio of gradients by uniform sampling is strongly biased to 1 in Fig. 5(a). A ratio of 1 means the gradient of samples are the same as the gradient of Euclidean distance, and samples with higher ratio are more informative.

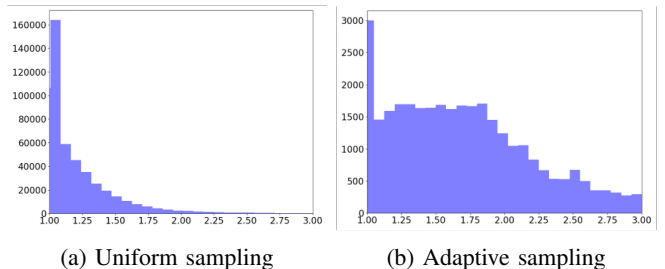


Fig. 5: Histogram of the ratio of true cost to Euclidean distance. High curvature regions would have a higher ratio. Uniform sampling heavily samples regions resembling Euclidean distance (ratio \approx 1), whereas adaptive sampling distributes the samples more evenly.

V. NEURAL NETWORK ARCHITECTURE

In this paper, for evaluation of suggested methods to learn cost-to-go functions of non-holonomic systems, we choose higher order function network (HOF) architecture proposed in [34] and applied to motion planning in our previous work [8].

The version we use for the present work, which we call the non-holonomic c2g-function network, is composed of two sub-networks; one sub-network is a function generating network by the HOF network and the other sub-network is the c2g-function (Fig. 6). In this paper, we use PointNet [35] as the encoder for the function generating network where we sample the obstacles in the workspace \mathcal{W} . The c2g-function network has three perceptron layers which have 256 neurons and a ReLU activation layer at each layers.

Once the network is trained, the function generating network encodes a point cloud of the workspace and outputs parameters of the c2g function network. The c2g-function network is instantiated with these output parameters. For the input of c2g-function network, sample configurations are concatenated with the goal configuration. Before the input layer of the c2g-function network, there is forward kinematics layer which computes sample configurations from sample control inputs.

A. Training

From the training dataset, we sample 50,000 pairwise configurations and corresponding ground-truth costs in one workspace instance. We input a workspace point cloud into the function generating network and construct the c2g-function network with the output from the function generating network. The constructed c2g-function network inputs concatenated pairwise configurations and it outputs predicted costs for sample configurations. Since the parameters of c2g-function networks are outputs of the function generating network, the Mean Squared Errors (MSE) between predicted costs and ground truth costs are backpropagated to the function generating network, which learns to output parameters of cost-to-go functions correctly to reduce MSE.

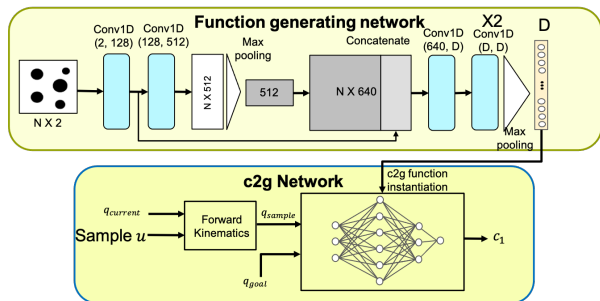


Fig. 6: Non-holonomic c2g-function network architecture

B. Trajectory Generation

We use cost-to-go function networks for path planning of non-holonomic systems. For the trajectory generation, first, control inputs are sampled and then a forward kinematics layer computes the next sample configurations with the current configuration and sampled control inputs. The next sample configurations are concatenated with the goal configuration and they are the input of the c2g-function network which outputs cost-values.

The network outputs a set of traversal costs from sample configurations to the goal configuration. It then removes infeasible control inputs such as collision with obstacles. The planner chooses the control input which has the minimum cost, and the configuration corresponding to this control input can be the next configuration. This routine repeats until the goal configuration.

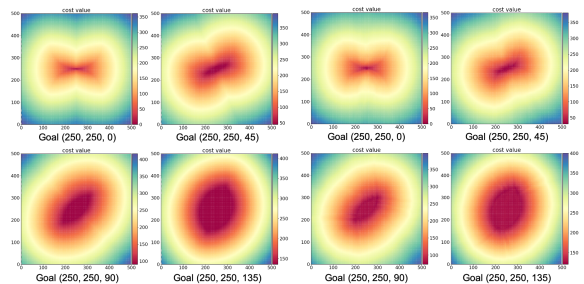
The planner’s stopping criteria for reaching the goal configuration is as follows: a) the current cost value is less than a threshold or b) the new configuration position has a smaller difference than a threshold and the orientation is less than a threshold. The sequence of current configurations can be the waypoint of the trajectories.

VI. RESULTS

This section presents experiments comparing our approach to existing planners in terms of trajectory length and computation time. In addition, to verify our sampling methodology, we show results obtained by trained networks with different sampling datasets, and verify the reliability of our approaches via a mobile robot simulator.

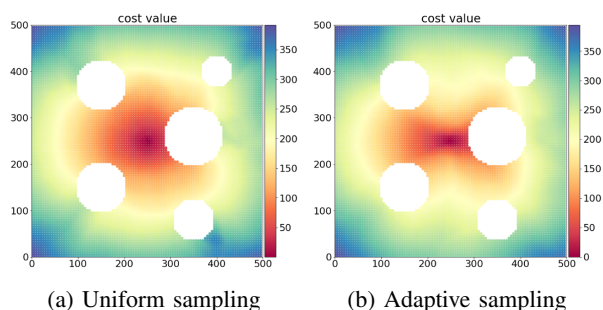
A. Learning of cost-to-go

Figure 7 shows a comparison of optimal ground truth cost-to-go by Reeds-Shepp curves and predicted cost-to-go by the network in an open environment with no obstacles. For the ground truth (Fig. 7(a)), we compute lengths of all Reeds-Shepp curves between grid points of (x, y, θ) and several different goal configurations. For the predicted cost-to-go (Fig. 7(b)), the trained network inputs the same grid configurations concatenated with a goal configuration. For visualization, Fig. 7 shows cross-sections of the cost-to-go at $\theta = 0$ for multiple goal configurations. Fig. 7 shows that the trained network predicts cost-to-go accurately over the entire continuous C-space. In addition, we can see how the cost changes with changing goal configuration. Note



(a) GT by Reeds-Shepp (b) Prediction by network

Fig. 7: Cost-to-go for various goal configurations in environments with no obstacles (a) ground truth (Reeds-Shepp curves) (b) the prediction by the trained network. For visualization, figures show cross-sections at $\theta = 0$ (Best viewed in color).



(a) Uniform sampling (b) Adaptive sampling

Fig. 8: Predicted cost-to-go by trained networks with two different datasets (a) uniform sampling dataset (b) adaptive sampling dataset. Figures show cross-sections of cost-to-go at $\theta = 0$ for the goal configuration at $(250, 250, 0)$. Adaptive sampling keeps high cost values behind obstacles and captures gradients well around the goal configuration (Best viewed in color).

that the prediction of cost-to-go for continuous configuration inputs is a strong advantage of learning of cost-to-go function network.

In cluttered environments, we compare our approach against a uniform sampling method. Fig. 8 shows comparison results by showing cross-sections of cost-to-go at $\theta = 0$ for the goal configuration at $(250, 250, 0)$. In the training result with uniform sampling (Fig. 8(a)), it has high cost-to-go behind obstacles to avoid obstacles. Note the lack of features around goal configuration. In contrast, the training result with the adaptive sampling (Fig. 8(b)) keeps high cost values behind obstacles and captures the changes of the gradient around the goal configuration. Since the changes of gradient are caused by the non-holonomic constraint, gradients around goal configurations are critical information to arrive at the goal configuration precisely.

B. Trajectory generation

We compare the performance of the c2g-network planner with other approaches, such as RRT, RRT*, and Reeds-Shepp methods in terms of trajectory length and computational time. In comparison, the RRT* planner is the same as the

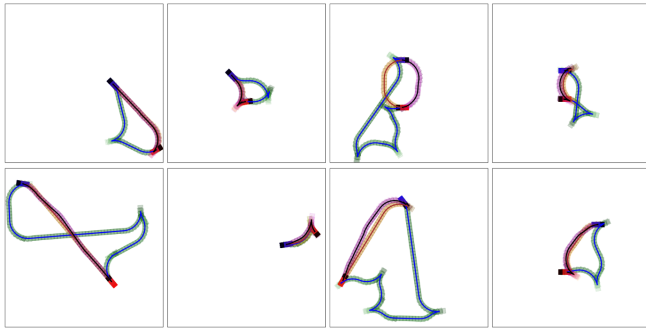


Fig. 9: Trajectories in the open space by RRT (blue), RRT* (orange), and c2g-network planner (magenta).

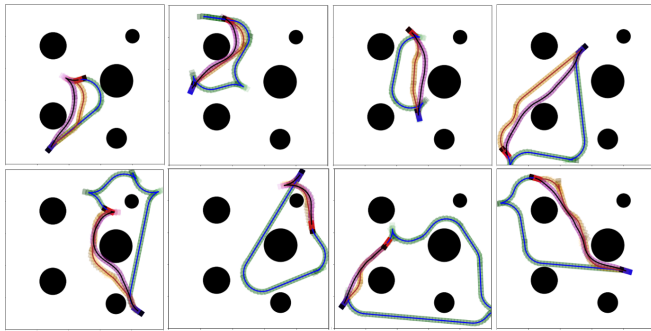


Fig. 10: Trajectories for various start and goal configurations in an environment with obstacles by RRT (blue), Reeds-Shepp curves (orange), and c2g-network planner (magenta) based on cost-to-go of Fig. 8(b).

method used for data generation. Although RRT* requires heavy computation, we compare ours with RRT* in terms of trajectory length. In addition, we apply 3% goal configuration biased sampling for RRT to accelerate it reaching the goal configuration. Reeds-Shepp curves are used for local planners of RRT and RRT* to connect between nodes. In the environment with no obstacle, we compare ours with optimal Reeds-Shepp curves. To speed up these comparison methods, we use Python API library of C++ codes by Open Motion Planning Library (OMPL) [36] for Reeds-Shepp curves [37].

Fig. 9 shows comparison results of trajectories by ours, RRT, and Reeds-Shepp curves. A start configuration is a blue rectangle, and a goal configuration is a red rectangle with orientations indicated by a black tip. Ours generates near-optimal trajectories which have almost the same length as the optimal Reeds-Shepp curves as shown in Fig. 9. The average trajectory length of ours is only 0.1% longer than the average trajectory length of optimal Reeds-Shepp curves and 50% less than the average trajectory length of RRT planner as shown in Fig. 12(a).

Fig. 10 shows generated trajectories with cost-to-go shown in Fig. 8(b) for multiple random start and goal configurations. Test start configurations, goal configurations, and test environments are not included in the training dataset. The trajectory generations are compared with RRT and RRT*. We can see that the trajectories by ours have shorter distances while avoiding obstacles compared to the slow RRT* planner

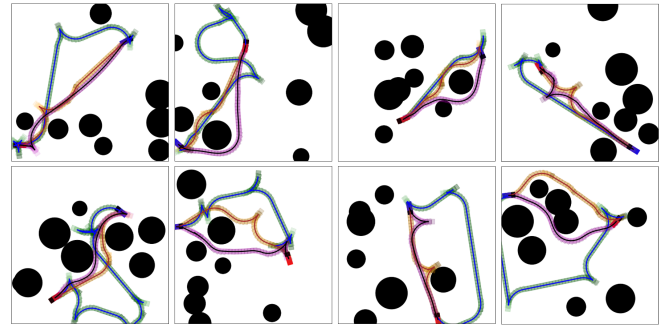


Fig. 11: Trajectories for various start and goal configurations in various cluttered environments by RRT (blue), RRT* (orange), and c2g-network planner (magenta).

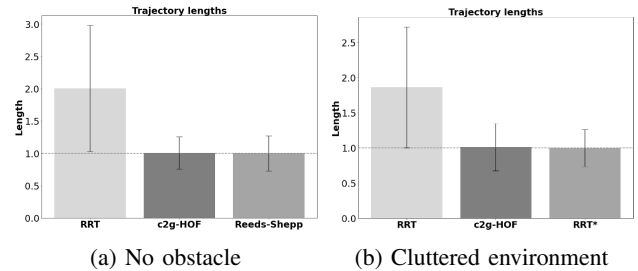


Fig. 12: Average trajectory length (a) trajectories in environments with no obstacles in Fig. 9 (b) trajectories in various cluttered environments in Fig. 11. The trajectory length is normalized by the average trajectory length of optimal Reeds-Shepp for the first case and RRT* for the latter.

or the inefficient RRT trajectories. Fig. 13(a) shows that computation time for ours (0.029 seconds) is two orders of magnitude faster than RRT (3.32 seconds) and RRT* (11.4 seconds).

We conduct quantitative comparison in various cluttered environments in terms of averages of computation time and trajectory length. Test start and goal configurations, and test environments are not included in the training dataset. Fig. 11 shows generated trajectories, and the average length of ours is only 1.1% longer than the average length of RRT* trajectories and 46% shorter than the average length of RRT trajectories (Fig. 12(b)). The average computation time is only 45ms compared to other approaches taking several seconds (Fig. 13(b)). We emphasize that ours has similar trajectory lengths to time-consuming RRT* and it takes less than 0.1 seconds for computation. Moreover, during trajectory generation, it does not need a local planner such as Reeds-Shepp curves which are used for connecting vertices in RRT and RRT*, while most planners require a local planner for satisfying non-holonomic constraints along with a global trajectory.

The success rate of our approach is 100% in cases of Figs. 9 and 10, and 98.5% in the case of Fig. 11.

In order to verify the effectiveness of the suggested sampling method, we test several trajectory planning tasks as shown in Fig. 14(b). Fig. 14(a) shows trajectories generated

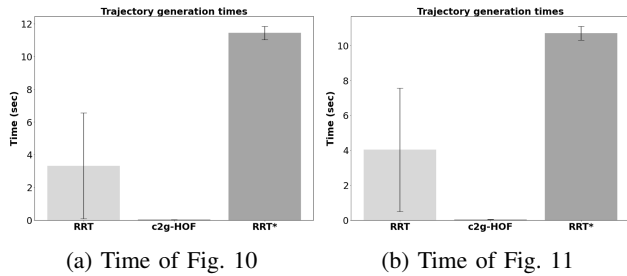


Fig. 13: Average trajectory generation time. Left to right: RRT, ours with adaptive sampling, RRT*

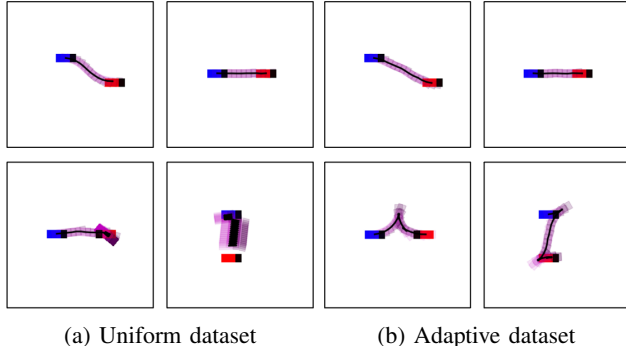


Fig. 14: Training with uniform (a) vs. adaptive sampling (b). Start configurations are marked blue and goal configurations (red) with the black part showing the orientation. As the curvature increases, uniform-sampling instances become less accurate.

by the network trained with the uniform sampling dataset and Fig. 14(b) shows trajectories generated by the network trained with the suggested sampling dataset. The top two figures show planning tasks in which cost-to-go values are similar to Euclidean distance from a start configuration (blue) to a goal configuration (red). In these tasks, both networks generate trajectories appropriately. In the bottom-left task, the relative angle between the start and the goal configurations is π and has a small relative distance in x - y plane. In this case, the trajectory based on the network trained with the uniform sampling dataset is just heading to the goal position without considering the orientation. However, the network trained with the suggested sampling dataset changes the orientation in the middle of the trajectory and arrives at the goal configuration correctly. In the bottom-right task, the goal configuration is parallel to the start configuration. The trajectory based on the network trained with the uniform sampling dataset and repeats inefficient forward and backward movements from the start configuration to the goal configuration. The network trained with the suggested sampling dataset generates a near-optimal path trajectory.

C. Simulation

In order to demonstrate the reliability of the generated trajectories, we conduct a simulation in test environments with a car with more realistic dynamics (Fig. 15(a)). In this simulation, the minimum turning radius of the mobile robot

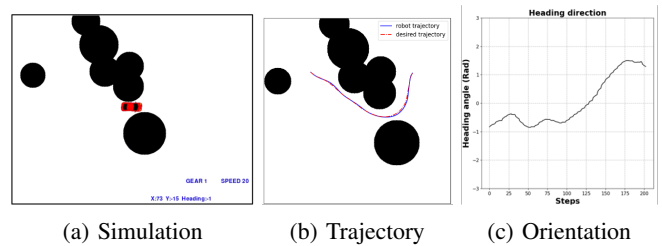


Fig. 15: (a) Simulation environment (b) the mobile robot trajectory (blue) tracking a trajectory (red) from c2g-network planner (c) Orientation of the mobile robot. We can see that the robot follows the desired trajectory smoothly without an abrupt change of states.

is $5.88m$ with $4.5m/s^2$ acceleration. The maximum speed is $11.25m/s$ and the mobile robot needs to stop and move again whenever it changes the direction. We apply a look-ahead controller for tracking the desired trajectory generated by the c2g-network planner to minimize the lateral error. As shown in Figs. 15(b) and 15(c), the mobile robot follows the desired trajectory well and generates smooth changes of orientation. Compared to Dubins or Reeds-Shepp curves which generate only minimum turning curves or straight lines, ours generates continuous steering control inputs. Therefore, the trajectories generated by ours are more reliable for real systems.

VII. CONCLUSION

This paper focused on learning based approaches for continuous cost-to-go function generation for non-holonomic systems. The high curvature regions of the optimal path manifold of non-holonomic systems make it difficult to represent them with uniform samples. We suggested an adaptive sampling approach based on the diversity of the gradient of the cost-to-go and showed that it leads to a successful representation of cost-to-go in C-space.

To show the effectiveness of our approach, we focused on the Reeds-Shepp car. We used a similar architecture to our recent work [8] where we presented cost-to-go generation networks for holonomic systems. We showed that the same network with uniform sampling is not effective for the Reeds-Shepp car. However, once trained with the presented adaptive sampling method, it generates the parameters of an accurate cost-to-go function network almost instantly. The planning based on the learned cost-to-go function network takes less than 0.1 seconds to generate near-optimal trajectories while other sampling-based planners take a few seconds. We also verified the reliability of generated trajectories in the mobile robot simulator. For future work, we plan to extend the approach to manipulators with smoothness constraints where sampling efficiency is critical due to the high dimension of the C-space.

REFERENCES

- [1] L. E. Dubins, "On curves of minimal length with a constraint on average curvature, and with prescribed initial and terminal positions and tangents," *American Journal of mathematics*, vol. 79, no. 3, pp. 497–516, 1957.

- [2] J. Reeds and L. Shepp, "Optimal paths for a car that goes both forwards and backwards," *Pacific journal of mathematics*, vol. 145, no. 2, pp. 367–393, 1990.
- [3] A. Koval and V. Isler, "Turning a corner with a dubins car," in *2019 International Conference on Robotics and Automation (ICRA)*. IEEE, 2019, pp. 8570–8576.
- [4] S. M. LaValle and J. J. Kuffner Jr, "Randomized kinodynamic planning," *The international journal of robotics research*, vol. 20, no. 5, pp. 378–400, 2001.
- [5] M. Kleinbort, K. Solovey, Z. Littlefield, K. E. Bekris, and D. Halperin, "Probabilistic completeness of rrt for geometric and kinodynamic planning with forward propagation," *IEEE Robotics and Automation Letters*, vol. 4, no. 2, pp. x–xvi, 2018.
- [6] K. Hauser and Y. Zhou, "Asymptotically optimal planning by feasible kinodynamic planning in a state–cost space," *IEEE Transactions on Robotics*, vol. 32, no. 6, pp. 1431–1443, 2016.
- [7] Y. Li, Z. Littlefield, and K. E. Bekris, "Asymptotically optimal sampling-based kinodynamic planning," *The International Journal of Robotics Research*, vol. 35, no. 5, pp. 528–564, 2016.
- [8] J. Huh, V. Isler, and D. D. Lee, "Cost-to-go function generating networks for high dimensional motion planning," *arXiv preprint arXiv:2012.06023*, 2020.
- [9] K. M. Lynch and F. C. Park, *Modern Robotics*. Cambridge University Press, 2017.
- [10] H. M. Choset, S. Hutchinson, K. M. Lynch, G. Kantor, W. Burgard, L. E. Kavraki, and S. Thrun, *Principles of robot motion: theory, algorithms, and implementation*. MIT press, 2005.
- [11] S. M. LaValle, *Planning algorithms*. Cambridge university press, 2006.
- [12] M. Pivtoraiko, R. A. Knepper, and A. Kelly, "Differentially constrained mobile robot motion planning in state lattices," *Journal of Field Robotics*, vol. 26, no. 3, pp. 308–333, 2009.
- [13] J.-C. Latombe, "Robot motion planning," 1991.
- [14] J.-P. Laumond et al., *Robot motion planning and control*. Springer, 1998, vol. 229.
- [15] H. G. Tanner, S. G. Loizou, and K. J. Kyriakopoulos, "Nonholonomic navigation and control of cooperating mobile manipulators," *IEEE Transactions on robotics and automation*, vol. 19, no. 1, pp. 53–64, 2003.
- [16] G. P. Roussos, D. V. Dimarogonas, and K. J. Kyriakopoulos, "3d navigation and collision avoidance for a non-holonomic vehicle," in *2008 American Control Conference*. IEEE, 2008, pp. 3512–3517.
- [17] Y. Tassa, N. Mansard, and E. Todorov, "Control-limited differential dynamic programming," in *2014 IEEE International Conference on Robotics and Automation (ICRA)*. IEEE, 2014, pp. 1168–1175.
- [18] A. Tamar, Y. Wu, G. Thomas, S. Levine, and P. Abbeel, "Value iteration networks," in *Advances in Neural Information Processing Systems*, 2016, pp. 2154–2162.
- [19] A. H. Qureshi, M. J. Bency, and M. C. Yip, "Motion planning networks," *arXiv preprint arXiv:1806.05767*, 2018.
- [20] J. J. Johnson, L. Li, F. Liu, A. H. Qureshi, and M. C. Yip, "Dynamically constrained motion planning networks for non-holonomic robots," *arXiv preprint arXiv:2008.05112*, 2020.
- [21] B. Ichter, J. Harrison, and M. Pavone, "Learning sampling distributions for robot motion planning," in *Proc. IEEE Int. Conf. Robot. Autom.*, 2018, pp. 7087–7094.
- [22] R. Kumar, A. Mandalika, S. Choudhury, and S. S. Srinivasa, "Lego: Leveraging experience in roadmap generation for sampling-based planning," *arXiv preprint arXiv:1907.09574*, 2019.
- [23] D. Molina, K. Kumar, and S. Srivastava, "Learn and link: Learning critical regions for efficient planning," in *2020 IEEE International Conference on Robotics and Automation (ICRA)*. IEEE, 2020, pp. 10 605–10611.
- [24] B. Ichter, E. Schmerling, T.-W. E. Lee, and A. Faust, "Learned critical probabilistic roadmaps for robotic motion planning," in *2020 IEEE International Conference on Robotics and Automation (ICRA)*. IEEE, 2020, pp. 9535–9541.
- [25] W. Zeng, W. Luo, S. Suo, A. Sadat, B. Yang, S. Casas, and R. Urtasun, "End-to-end interpretable neural motion planner," in *Proceedings of the IEEE/CVF Conference on Computer Vision and Pattern Recognition*, 2019, pp. 8660–8669.
- [26] A. Katharopoulos and F. Fleuret, "Not all samples are created equal: Deep learning with importance sampling," in *International conference on machine learning*. PMLR, 2018, pp. 2525–2534.
- [27] Y. Fan, F. Tian, T. Qin, J. Bian, and T.-Y. Liu, "Learning what data to learn," *arXiv preprint arXiv:1702.08635*, 2017.
- [28] N. M. Amato, O. B. Bayazit, L. K. Dale, C. Jones, and D. Vallejo, "Obprm: An obstacle-based prm for 3d workspaces," in *Proc. Int. Workshop on Algorithmic Foundations of Robotics (WAFR)*, 1998, pp. 155–168.
- [29] S. Rodriguez, X. Tang, J.-M. Lien, and N. M. Amato, "An obstacle-based rapidly-exploring random tree," in *Proc. IEEE International Conference on Robotics and Automation (ICRA)*, 2006, pp. 895–900.
- [30] H.-Y. Yeh, S. Thomas, D. Eppstein, and N. M. Amato, "UOBPRM: A uniformly distributed obstacle-based PRM," in *Proc. IEEE/RSJ International Conference on Intelligent Robots and Systems (IROS)*, 2012, pp. 2655–2662.
- [31] J.-P. Laumond, S. Sekhavat, and F. Lamiroux, "Guidelines in nonholonomic motion planning for mobile robots," in *Robot motion planning and control*. Springer, 1998, pp. 1–53.
- [32] P. K. Agarwal, T. Biedl, S. Lazard, S. Robbins, S. Suri, and S. Whitesides, "Curvature-constrained shortest paths in a convex polygon," *SIAM Journal on Computing*, vol. 31, no. 6, pp. 1814–1851, 2002.
- [33] S. Karaman, M. R. Walter, A. Perez, E. Frazzoli, and S. Teller, "Anytime motion planning using the RRT*," in *IEEE Int. Conf. Robot. Autom.*, 2011, pp. 1478–1483.
- [34] E. Mitchell, S. Engin, V. Isler, and D. D. Lee, "Higher-order function networks for learning composable 3d object representations," in *International Conference on Learning Representations*, 2019.
- [35] C. R. Qi, H. Su, K. Mo, and L. J. Guibas, "Pointnet: Deep learning on point sets for 3d classification and segmentation," in *Conf. Comp. Vision Pattern Recognition*, 2017, pp. 652–660.
- [36] I. A. Şucan, M. Moll, and L. E. Kavraki, "The Open Motion Planning Library," *IEEE Robotics & Automation Magazine*, vol. 19, no. 4, pp. 72–82, December 2012, <https://ompl.kavrakilab.org>.
- [37] G.-H. Liu, "Reeds shepp path library," 2016, available online at <https://github.com/ghliu/pyReedsShepp>.